Acta Materialia 194 (2020) 558–564

Contents lists available at ScienceDirect

Acta Materialia

journal homepage: www.elsevier.com/locate/actamat

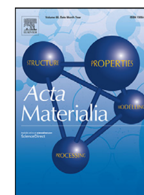

Full length article

Optical characterization of grain orientation in crystalline materials

Bernard Gaskey[a], Ludwig Hendl[a,b], Xiaogang Wang[a], Matteo Seita[a,c,*]

[a] School of Mechanical and Aerospace Engineering, Nanyang Technological University, Singapore
[b] Department of Physics, University of Hamburg, Hamburg, Germany
[c] School of Materials Science and Engineering, Nanyang Technological University, Singapore

A R T I C L E I N F O

Article History:
Received 26 March 2020
Revised 9 May 2020
Accepted 12 May 2020
Available online 20 May 2020

Keywords:
Directional reflectance
Crystal orientation mapping
High-throughput characterisation
Optical metallography

A B S T R A C T

Characterizing crystallographic orientation is essential for assessing structure-property relationships in crystalline solids. While diffraction methods have dominated this field, low throughput and high cost limit their applicability to small, specialized samples and restrict access to well-funded research institutions. We develop a complementary method that expands applicability and broadens access. We demonstrate crystal orientation mapping over centimeter-scale surfaces using nothing more than a conventional optical microscope and commercial laptop. Our approach relies on a novel analysis method that correlates crystal lattice orientation to optical reflectance of specially etched surfaces. We successfully apply the method to metal and semiconductor surfaces. The simplicity, low cost, and enhanced sample throughput of our method promise to expand the availability of crystallographic orientation mapping significantly, making it readily available in education as well as academic research and industrial settings.

© 2020 The Authors. Published by Elsevier Ltd on behalf of Acta Materialia Inc. This is an open access article under the CC BY-NC-ND license (http://creativecommons.org/licenses/by-nc-nd/4.0/)

1. Introduction

Cornerstones of modern technology, such as miniaturized electronics, efficient energy harvesting devices, and high-performance aerospace engines, exist due to advances in crystalline materials. The majority of these materials are polycrystals—aggregates of crystalline grains with different atomic lattice orientations [1]. The properties of a polycrystal depend on the size [2,3], shape [4,5], and the relative lattice orientations of its constituent grains [6]. Assessing these quantities throughout the lifetime of a material—from its design in the laboratory, through the qualification of parts for service, and the analysis of eventual failure—is vital both for predicting the performance of existing materials and for designing new ones.

Measuring the orientations of individual grains in a polycrystal by electron microscope was an important milestone in the development of crystallographic characterization techniques. Kikuchi diffraction occurs when high-energy electrons strike a crystalline surface and scatter back, projecting high density scattering bands along directions that are related to the structure and orientation of the crystal [7,8]. This phenomenon forms the basis of electron backscatter diffraction (EBSD), which has become the gold standard for characterizing the surface crystallography of crystalline solids [9,10]. However, EBSD analysis of surfaces is a time- and capital-intensive practice, limited to small, specialized samples. We present a new method for assessing crystal orientation based on directional reflectance microscopy (DRM) that avoids these shortcomings. Rather than diffraction from the atomic lattice, this technique is based on optical reflection from orientation-dependent features on the surface [11].

Many materials can be etched to preferentially remove small amounts of material from the surface of specific crystallographic planes [12]. The resulting structure is dominated by microscopic facets, which inherit their direction and geometry from the underlying atomic lattice orientation [13,14]. This relationship provides the fundamental connection between surface structure and crystallography which conveys lattice orientation information to a scale that is visible by optical microscopy. By introducing a novel method to analyze light scattering from these structures, we employ DRM to map crystal orientation across the surface of nickel (Ni) and silicon (Si). Using this technique, DRM becomes a powerful new characterization tool for a variety of materials.

2. Methods

We demonstrate grain orientation mapping by means of DRM on two samples; a >99% pure Ni coin and a fragment from a 1 mm thick polycrystalline Si solar cell. We prepared the surface of both Ni and Si samples by mechanical polishing. The samples were chemically etched to generate the surface features for DRM. The Ni sample was immersed in an unstirred chemical bath of Marble's reagent (10g $CuSO_4$ dissolved in 50 mL 36% hydrochloric acid and 50 mL deionized water) for 180 minutes at room temperature, and the Si wafer was

* Corresponding author.
E-mail address: mseita@ntu.edu.sg (M. Seita).

https://doi.org/10.1016/j.actamat.2020.05.027
1359-6454/© 2020 The Authors. Published by Elsevier Ltd on behalf of Acta Materialia Inc. This is an open access article under the CC BY-NC-ND license (http://creativecommons.org/licenses/by-nc-nd/4.0/)

immersed in unstirred 13wt% potassium hydroxide solution for 40 minutes at 40°C. We characterized etch-induced surface structures and grain orientation by means of scanning electron microscopy (JEOL 7600F field emission microscope) and EBSD (Oxford instruments Nordlys 2S detector), respectively. EBSD measurements were taken with 15 μA emission current, 20 kV accelerating voltage, and a 15 μm step size.

The apparatus used for DRM measurements includes a sample stage, a fixed microscope focused on the stage from above, and a moveable arm which holds the light source. The configuration is shown schematically in Fig. 1c. We varied the direction of incoming light by means of two motors, which control the light source azimuthal angle, φ, and elevation angle, θ. We used a Cold White Collimated LED for Olympus by Thorlabs as light source, and an Olympus SZ6145 equipped with a DMK 33UX250 CMOS black and white camera as microscope. To automate data gathering, we used an in-house developed Matlab software interface that controls the angular motors and microscope camera. We collected a set of 72 images taken in 5° increments across φ. For each φ, we varied the elevation θ between 5° and 70° above sample horizon in steps of 2.5°. A complete DRM dataset consists of 1944 micrographs—one for each (φ, θ) illumination direction. To compensate for uneven light intensity, we acquired a corresponding set of micrographs taken after replacing the sample with a uniform white reflector. We used this additional dataset as a background for normalization [16]. As the elevation of the light source increases, the intensity of illumination on the sample also increases. In order to maintain ideal contrast in micrographs taken across θ, we adjusted the exposure time of the camera to compensate for the variation in illumination. The ideal light intensity in a unit area of the surface varies according to

$$\mathrm{I} = \sin(\theta) \tag{1}$$

so we adjusted the exposure time by

$$\mathrm{E} = \frac{C}{I} = C \cdot \csc(\theta) \cdot \sin(45^\circ) \tag{2}$$

where C is the empirically determined optimal exposure time when θ = 45°. This method assures approximately constant contrast between features in micrographs taken at different incident light angles.

3. Results

3.1. Crystallographic directional reflectance

In the face centered cubic crystal structure of Ni, {111} planes of close-packed atoms have the slowest etching rate due to their minimal surface energy. During etching, pits consisting of {111} facets preferentially develop across the entire surface. Fig. 1a shows the corrugated surface of an etched Ni grain, which is covered by two types of {111} facets. When monodirectional light strikes such a surface along the normal direction, much of it will undergo specular reflection from these facets and a much lower proportion will reflect in other directions. Each facet orientation will reflect light in only one direction, so grains that share the same surface structure will also have the same specular reflection pattern—which we refer to as directional reflectance. The directional reflectance corresponding to the surface in Fig. 1a is visualized in Fig. 1b as a hemisphere above the surface surrounding the point of illumination, with intensity

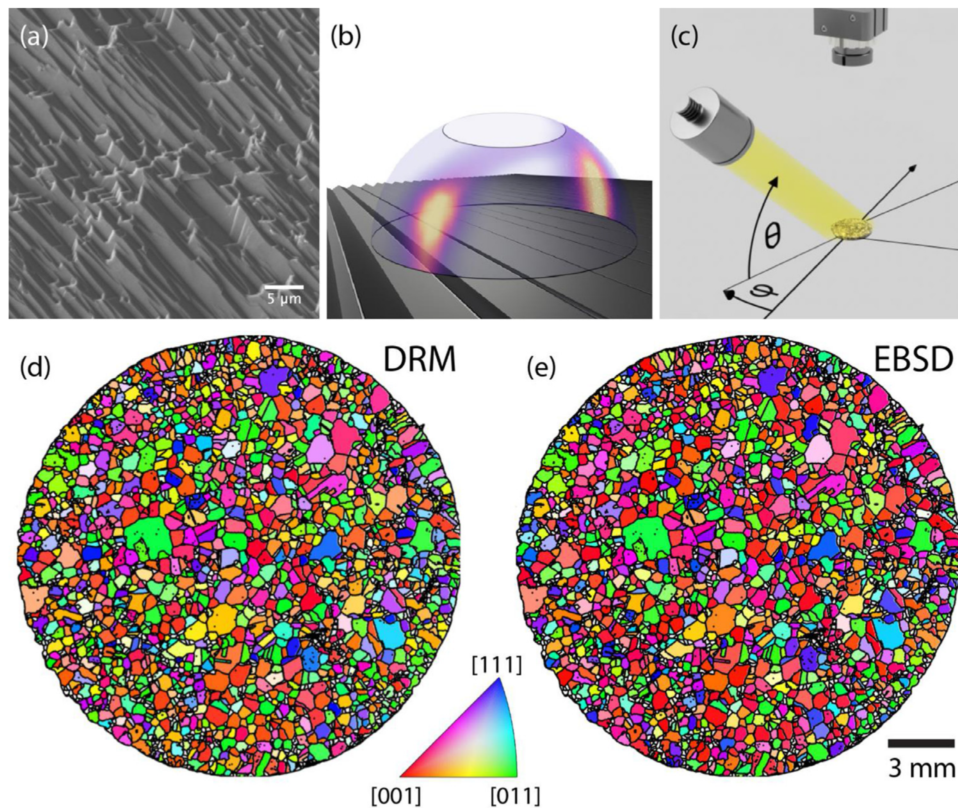

Fig. 1. (a) SEM micrograph of the etched Ni surface showing faceting dominated by two main {111} crystal surfaces. (b) A 3D representation of the corrugated surface from (a) with the corresponding angular reflectance superimposed. The bright regions of reflectance intensity highlighting two primary reflection directions which correspond to specular reflection from the two main facets. (c) A schematic representation of the DRM apparatus used to measure the reflectance distribution shown in (b) by changing the position of the light to vary the incident angle in terms of two angular coordinates (φ, θ). (d) Surface normal texture map produced by analysis of DRM measurements on a 2cm coin of polycrystalline Ni. (e) The same texture map produced by EBSD.

related to the reflectance in each direction. The two bright spots correspond to the specular reflections from the {111} facets. Directional reflectance is a subset of the bidirectional reflectance distribution function which provides information about the orientation and geometry of these reflecting features across the surface [15].

Designing a measurement apparatus based on an array of detectors to compare reflectance in many directions simultaneously is complex. Instead, taking advantage of the reciprocity of reflections, we capture the angle-dependent surface reflectance by rotating the light source relative to the fixed sample and camera. This implementation, shown schematically in Fig. 1c, forms the basis of directional reflectance microscopy (DRM)[16]. DRM involves capturing a series of optical micrographs of the sample illuminated from different directions. Through mathematical analysis of directional reflectance across the series of micrographs (detailed in Section 3.2), we identify grains and measure their three-dimensional (3D) crystallographic orientation (as explained in Section 3.3).

The signature output from EBSD is a map showing the crystal lattice orientation at each pixel, color coded based on the inverse pole Fig. of the crystal structure under analysis. By convention, [100]-oriented grains are colored red, [110] grains green, and [111] grains blue. Intermediate orientations are represented by colors that interpolate between these extremes. In Fig. 1, we show the grain map of a 2 cm diameter polycrystalline Ni coin that was calculated by DRM analysis (Fig. 1d) compared to one produced using EBSD measurements (Fig. 1e). The two maps are generally in very good agreement. The DRM map took around 30 minutes to compile using a desktop apparatus without atmosphere control. The EBSD map could take several hours depending on the EBSD camera and settings (here ~6 hours) using professionally maintained commercial instrument and must be conducted in high vacuum.

3.2. Quantitative analysis of directional reflectance

A DRM dataset contains a series of micrographs where the angle of incoming light for each micrograph is defined by azimuthal and elevation coordinates (φ and θ, respectively). Because the sample and microscope detector are both immobile, there is no need to refocus the image or perform image registration within a dataset; the same point on the sample will appear in the same pixel of each micrograph. The DRM dataset forms a 4-dimensional matrix of reflectance where each element is defined by its Cartesian coordinates on the sample surface (2-dimensionally) and the incident light angle (by the two angular parameters). The individual micrographs are slices of this data space at fixed φ and θ. The data can also be sliced holding the position constant, giving a description of angle-dependent reflectance for a single pixel or group of pixels (i. e. a grain) in each micrograph. We call this representation a directional reflectance profile (DRP). DRPs quantify the intensity of light reflected along the sample normal as a function of the incident illumination angle. Fig.s 2a, 2d, and 2g show example DRPs from three different grains. DRPs main features are bright specular reflection peaks centered at specific angles as well as dimmer bands connecting the peaks, which we attribute to the curvature of the edges between {111} facets.

The angular coordinates of each peak can be used to recover the normal vector to the associated {111} surface facet [17]. The in-plane component of the vector, $\varphi_{<111>}$, is the φ-coordinate of the reflectance peak center, φ_P, while the out-of-plane component, $\theta_{<111>}$, is given by

$$\theta_{\langle 111 \rangle} = \frac{1}{2}(90 + \theta_P) \tag{3}$$

where θ_P indicates the θ-coordinate of the reflectance peak center.

The θ measurement angles in DRM are practically limited to $5^\circ \leq \theta \leq 70^\circ$. At shallower angles, light is attenuated by self-shadowing between features on the sample surface. At higher angles, the light source interrupts the light path to the microscope. This range of measurement angles corresponds to $47.5^\circ \leq \theta_{<111>} \leq 80^\circ$, limiting the visibility of {111}-facet peaks for crystals with out-of-plane orientation near [001] and [111] (e.g. Figs. 2a and 2d, respectively). In these cases, the center of a reflection peak is not visible, so calculating orientation is not possible solely by identifying peaks.

We also consider the reflectance bands which follow great circles that connect <111> poles of the crystal via <101> directions, as shown schematically in Figs. 2b, 2e, and 2h for the three principal crystal orientations. In these schematics, blue and green facets correspond to {111} and {101} planes, respectively. Because peaks and bands all lie along the same family of great circles, we compile the total reflectance along many possible great circles in the DRP to identify those with highest intensity. This group of great circles are all related by the symmetries of a cubic crystal, so they are equivalent with respect to crystal orientation. We apply a discrete implementation of the Funk-Radon transform (FRT), which converts a DRP parametrized by φ and θ into a function of great circle angular coordinates (y_1, y_2). The FRT is the polar coordinate version of the linear Hough transform operation used to index diffraction patterns in EBSD [9]. Mathematically, the FRT is expressed as

$$\boldsymbol{FRT} f(x) = \int_{u \in C(x)} f(u) ds(u) \tag{4}$$

where ***FRT*** *f(x)* denotes the FRT of a function, *f(x)*, which expresses the reflectance intensity in the DRP. The basis of great circles along which to integrate is defined on the sphere S^2. Each individual great circle *C(x)* is formed by a set of vectors, *u*. This set is defined in terms of the normal vector *x* by

$$C(x) = \left\{ u \in S^2 \middle| x \cdot u = 0 \right\}. \tag{5}$$

The FRT integral is evaluated by integrating all *u* for each great circle *C(x)* in the set of great circles of interest, where *f(u)* is the value of the function along the direction of *u* and *ds(u)* is the arc length of the great circle associated with *u*. In our implementation, we parameterize *x* by the elevation, y_1, and azimuthal, y_2, angles, similarly to the two angles varied during DRM. Some great circles can be omitted from our FRT because they will never intersect the domain of the DRP. One such instance is the great circle that coincides with the equatorial line in the sample reference frame. Thus, we only identify the DRM angle pairs corresponding to each remaining great circle. Using this correspondence, we populate a fourth order tensor, *T*, describing the discrete FRT, *F*, from a DRP, *R*, by

$$F_{y_1, y_2} = T_{y_1, y_2, \varphi, \theta} \cdot R_{\varphi, \theta}. \tag{6}$$

In general, each point on the DRP will transform into a curve on the FRT containing all the great circles which intersect at that point. A pair of points in the DRP transforms in two curves in the FRT, whose intersection identifies the great circle connecting the two points. An arc on the DRP transforms to a standalone peak in FRT space. Once *T* has been computed, we apply Eq. 6 to transform any DRP into the corresponding FRT. The FRT matrix can be plotted to visualize the integrated intensity along great circles in a y_1-y_2 Cartesian space. Figs. 2c, 2f, and 2i show the FRT matrices corresponding to the DRPs in Figs. 2a, 2d, and 2g, respectively. We identify the great circle which contains the most total reflection intensity in a DRP by locating the global maximum in the corresponding FRT. Using the FRT to identify this great circle has the advantage of increasing the orientation-dependent information that can be extrapolated from DRPs by considering reflectance peaks and reflectance bands together, as opposed to using fitting-based methods on DRPs directly.

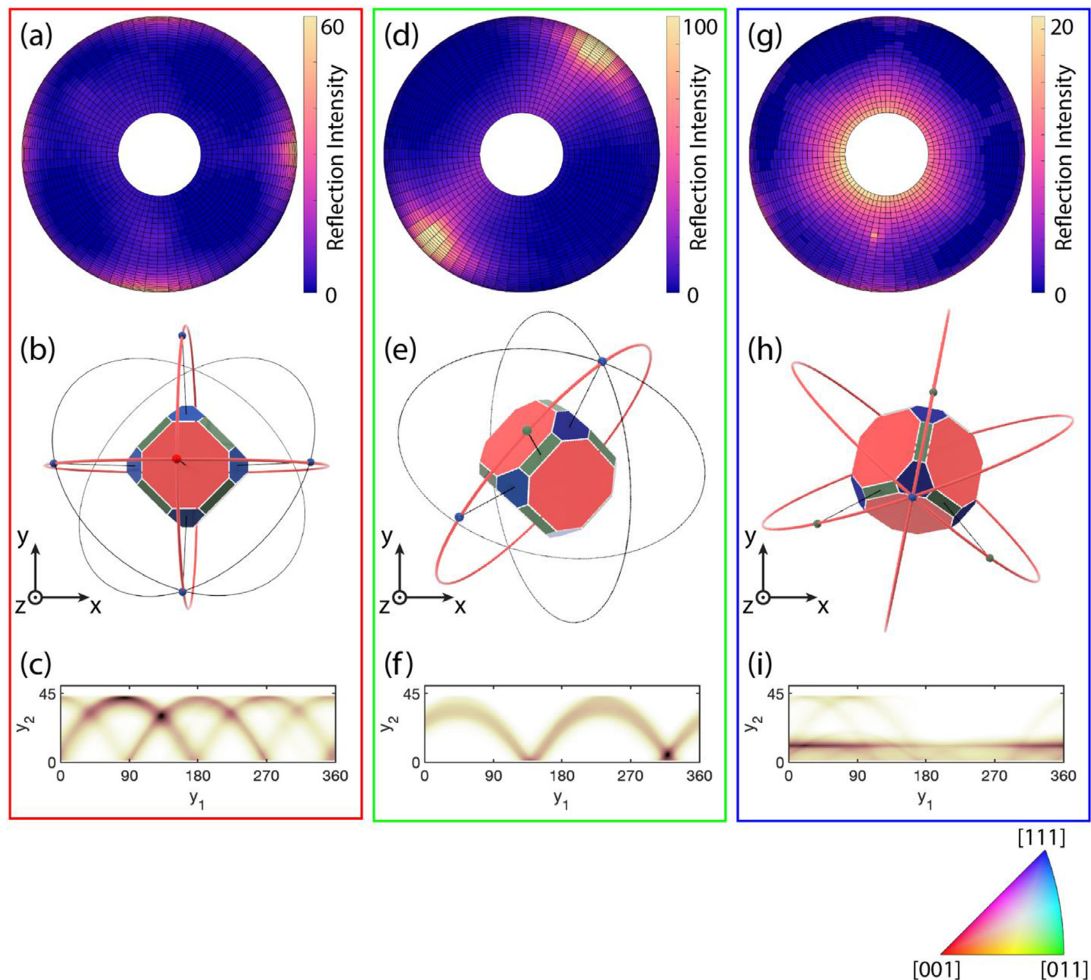

Fig. 2. The relationship between directional reflectance, crystal lattice orientation, and Funk-Radon transform for three exemplary Ni grains. (a) DRP from a [001]-oriented grain containing 4 notable reflectance peaks visible at the DRP edges; (b) corresponding crystal orientation showing that the reflectance maxima are associated with <111> directions (in blue); and (c) corresponding FRT exhibiting 4 curves associates with the 4 reflectance peaks in the DRP. (d) DRP from a [101]-oriented grain similar to that shown in Fig. 1a and 1b, with only one reflectance band associated with (e) a single great circle linking the two <111> directions and giving rise to (f) a single maximum in the FRT. (g) DRP of a [111]-oriented grain with weak 6-fold symmetry in the DRP compared to (h) a 3-fold symmetry of the crystal lattice itself, and (i) a single broad feature in the FRT. DRPs like this one are the most difficult to index properly due to the lack of well-defined peaks or bands, and the ambiguity brought about by the symmetry.

3.3. Calculating grain orientation from directional reflectance

We segment a DRM dataset into the materials constitutive grains using a Canny edge-detection algorithm described previously [36]. For each grain, we take the median value of the constituent pixels to build a representative DRP and perform the FRT operation according to Eq. 6. The DRP and FRT together form the input to the orientation indexing algorithm.

Three angles are required to specify the 3D orientation of a crystal. The FRT maximum provides the coordinates (y_1, y_2) of the maximum great circle. The third angle describes where on that great circle a $\langle 111 \rangle$ vector can be found. We use different algorithms to calculate this third angle, depending on features of the DRP and FRT. If the FRT has a second local maximum, we use the intersection between this second great circle and the global maximum, which lies along a $\langle 111 \rangle$ vector. In situations where only one great circle can be found, we examine the DRP directly and derive the third angle from the (φ, θ) coordinates of the reflectance peak using Eq. 3. To provide additional precision, we interpolate the location of the reflectance peak with a simple quadratic fit independently along both φ and θ. Grains with reflectance peaks that lie near the edge or outside the viewing area of the DRP (such as those in Figs. 2a and 2g) require specialized analysis to accurately calculate the location of the peak center or correctly identify the optimal great circle.

When reflectance peaks fall below the low-θ edge of the DRP—as it is for near [001]-oriented grains—only the peaks tail is visible (Fig. 2a). Plotting the reflection intensity in this tail as a function of θ shows how the reflectance decays as a function of distance from the reflection center. A Lorentzian or Cauchy distribution empirically fits this decay well in most cases, and the center of the peak can be estimated based on the fitting parameters of the distribution.

When the DRP maximum occurs at high-θ angles—as it is for near [111]-oriented grains—the peak center falls within the gap in the DRP domain caused by obstruction of the camera (Fig. 2g). In this case, the most important features on the DRP are the bands which originate from this central reflectance peak. These bands lie on relevant great circles, but they can be overshadowed in the FRT by the high-θ reflectivity around the peak, leading to a spurious maximum in the FRT. To simplify the analysis, we consider a binarized DRP that assumes value zero unless the intensity at a point is a local maximum along the φ direction. This operation yields a DRP with ones primarily along the centers of reflectance bands. We smoothen the binarized DRP by Gaussian blurring to limit measurement noise and apply the FRT operation. This FRT specifically highlights the bands that intersect at the obscured reflectance peak with much greater contrast and it always contains at least two maximal great circles from which the angular location of the <111> vector can be estimated accurately.

Any of these methods yields a pair of rotation angles (y_1, y_2) specifying a great circle in the FRT, and the vector direction of [111] which lies along the same great circle. The great circle also intersects $[11\bar{1}]$, so the normal vector to the plane containing the great circle is the cross product of these two vectors, $[1\bar{1}0]$. We calculate the components of this vector from the great circle angles. Rotating [111] by 70.5° about $[1\bar{1}0]$ gives $[11\bar{1}]$. The sum of [111] and $[11\bar{1}]$ lies along the [001] crystal axis. Similar vector manipulations give the orientations of the basis vectors for the crystal coordinate system [100], [010], and [010], which can then be converted into the standard Euler angle triplet for that grain by well-documented methods [18].

In contrast to EBSD orientation mapping, the FRT-based methodology does not require material-specific parameters, such as the lattice constant, to index DRPs. Instead, it depends exclusively on reflection from surface facets with known crystallography. The same mathematical framework applied to Ni is also effective on a Si sample etched to induce {111}-faceted pits. Compared to Ni (Fig. 2), Si DRPs (Fig. 3a) exhibit sharper {111} specular reflections connected by brighter reflectance bands. The out-of-plane and in-plane grain orientation maps are shown in Figs. 3b and 3c.

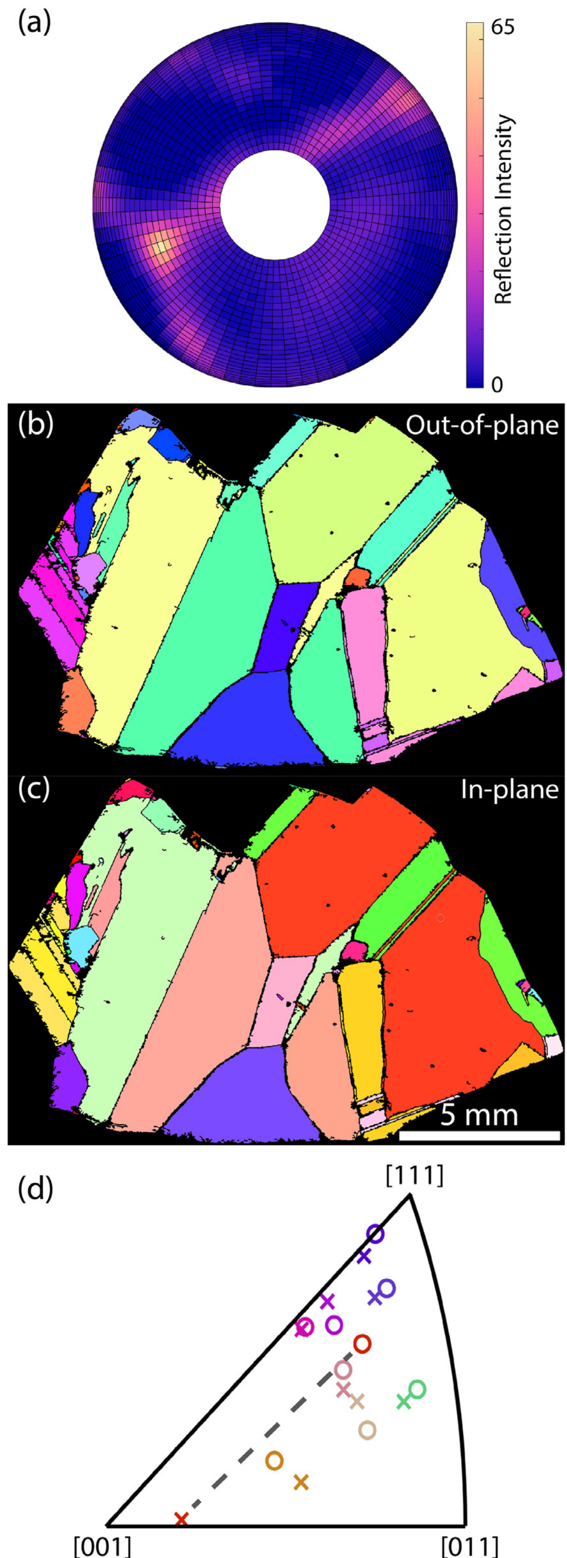

Fig. 3. (a) The DRP of a Si grain showing very concentrated bright directional reflectance features from {111} facets but retaining the bands connecting them. (b) In plane and (c) out of plane inverse pole Fig. grain maps produced by DRM for a fragment of a Si solar cell. Together these maps provide full orientation information about the grains in this sample. (d) Visualization of the orientation difference in individual grains measured by EBSD (circles) and DRM (crosses) for a random sample of grains in this Si sample. One grain (orange markers) has been indexed incorrectly by DRM, while the others are within a few degrees of the EBSD orientation.

3.4. Error quantification

The DRM maps presented in Figs. 1 and 3 index the DRP for every grain, but they include discrepancies with maps acquired by EBSD. We quantified these differences by comparing EBSD and DRM orientation measurements on a grain by grain basis. Using the grain boundary map from DRM, each grain was assigned an orientation based on the representative DRP for that grain. Each grain was also assigned a representative EBSD orientation taken from the grain with the nearest center in the EBSD dataset. To correct for image distortion between the two measurement techniques, we manually registered the two data sets in several sections. We then calculated the smallest angle rotation required to bring the two orientations from DRM and EBSD into coincidence, which we refer to as the angular difference between the two methods.

Fig. 3d shows this metric for 9 Si grains, plotted in an inverse pole figure. In general, we find good agreement between DRM and EBSD orientation measurements. Because of the poor statistics in the Si sample, however, we base the DRM error quantification on the Ni sample. Fig. 4a shows that the angular difference between DRM and EBSD is primarily distributed between 0° and 10° and centered around 4°. Relatively few grains were indexed unpredictably, with large random angular difference. We attribute these cases to inaccuracies in the grain boundary map, which causes a single DRP to contain reflectance peaks from several smaller physical grains. The additional peak around 60° originates specifically from grains near [111] out-of-plane texture (Fig. 4b), for which the 6-fold symmetry of three great circles passing through the DRP causes an in-plane rotation ambiguity (Fig. 2g). Aside from this special case, the optical orientation measurements enabled by DRM are broadly accurate. The largest contribution to the angular difference spread shown in Fig. 4a comes from grains with out-of-plane texture in-between [111] and [001] (Fig. 4b), whose DRPs contain one single reflectance peak. In these cases, the correct identification of the maximum great circle largely depends on the brightness of reflectance bands. A low signal-to-noise ratio in these DRPs may yield diffuse FRT peaks and thus inaccurate indexing of crystal orientation.

More complex indexing strategies could both avoid ambiguities when indexing high-symmetry crystal orientations as well as improve the accuracy of DRM measurements. One such strategy is to apply a physics-based forward model for indexing DRPs [19,20].

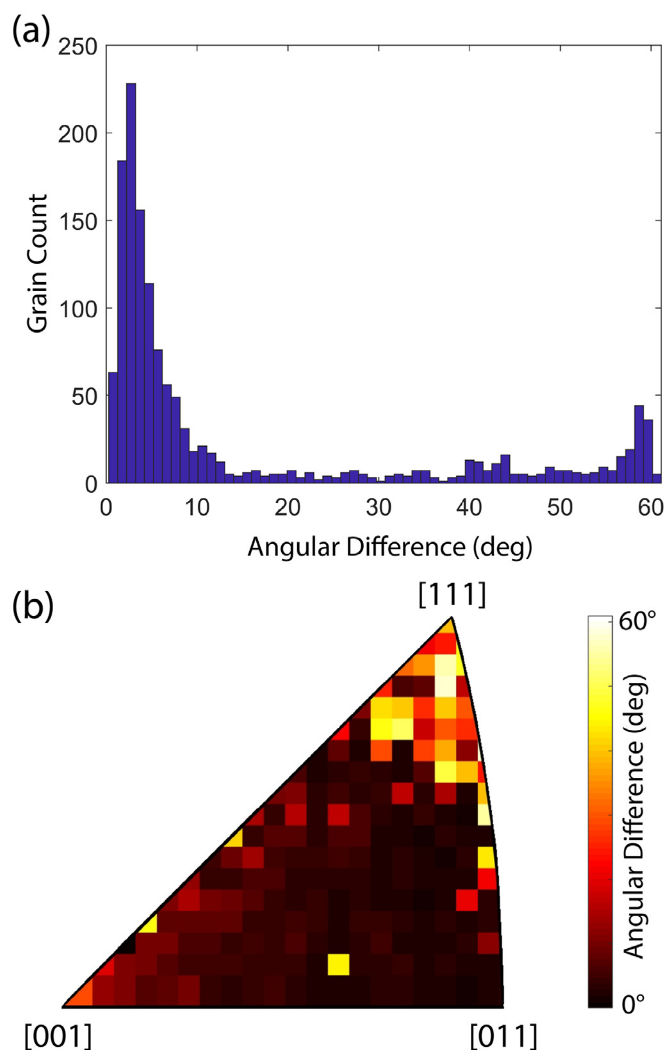

Fig. 4. (a) Quantification of differences between DRM and EBSD orientation measurements for the Ni maps shown in Figs. 1d and 1e. The angular difference refers to the smallest total rotational angle that brings the two measurements into coincidence. (b) The same difference distribution is plotted as a function of out-of-surface texture and shows the majority of errors cluster around [111].

Comparing a measured DRP to a dictionary of simulated ones to find the best match has the advantage of considering the directional reflectance signal holistically. Ambiguities may be resolved by distinguishing the intensity of different reflectance bands and the measurement accuracy may be improved by evaluating the DRP as a whole, as opposed to extracting individual features such as a single reflectance band and peak pair. Another approach is to employ emerging data science tools, such as deep learning, which could self-identify new methods for interpreting directional reflectance data [21].

Although DRM does not require a mirror-like surface finish, the etching of the surface is an important parameter. For materials including commonly used metals, metal alloys, and semiconductors, a large body of literature provides etching recipes and insight into the crystallography of the resulting surface, which can be directly applied to DRM surface preparation [12]. DRM can be relatively robust to variations in etching behavior as long as the same facet types are favored. Our results on Si demonstrate that variations in etch pit size and distribution do not directly compromise crystal orientation calculations, although they modify the reflectance distribution of individual DRPs.

4. Discussion

While DRM orientation mapping could become a valuable low-cost alternative to EBSD, there are areas where the latter will remain the method of choice. Because of the diffraction limit of light [22], the smallest surface feature that can generate directional reflectance according to specular reflection rules is on the order of half a micrometer [23]. To form a complete DRP, several such features must fit on the surface of each grain, so the grain diameter must be several times greater than this limit to be suitable for DRM orientation mapping. In samples with finer microstructures, DRM may still have utility as a complimentary tool to EBSD, for example to rapidly identify regions of interest that require further high-resolution investigation. The large-scale microstructure heterogeneity that is commonly found in additively manufactured metals makes the common research practice of taking representative EBSD measurements from a small subset of a sample problematic [24]. DRM could provide a particularly valuable tool to rapidly assess microstructure across entire parts [25,26]. DRM could also be applied to reconstruct the 3D microstructure of large samples using repeated measurements and etching steps, providing a larger scale than existing EBSD-based serial sectioning datasets [27,28].

Several other methods to measure crystallographic orientation have been proposed as alternatives to EBSD. Statistical texture can be inferred using ultrasound methods to identify changes in elastic behavior associated with crystal orientation [29,30]. The basal texture of titanium can be inferred using its unique interaction with polarized light [31]. Taking advantage of the crystallographic relationships of etched surfaces, the topography of etch pits have been measured directly by coherence scanning interferometry [32,33]. Recently, 3D mapping of crystal orientation has been accomplished in some materials using Raman microscopy [34]. However, all the above-mentioned approaches are each limited to specific materials, lack spatial resolution, or have low throughput. In contrast, DRM has unique promise to overcome these hurdles and provide spatially resolved orientation information over large areas of any material for which a crystallographic etchant exists. In cases where the reduced number of specular reflections and reflectance bands make DRPs indexing difficult—such as in non-cubic, low-symmetry materials—combining multiple DRM data sets acquired using different etching conditions that favor the formation of facets with different crystallography may be a suitable solution.

DRM can provide previously impossible large-scale characterization at many stages of the fabrication process for crystalline components. Because the rate of DRM measurements is independent of overall sample dimensions, this technique lends itself to characterizing entire multi-crystalline Si solar cells or turbine blades at the same rate as samples presented in this work. DRM is uniquely suited to inline quality assurance and adaptive manufacturing owing to the flexibility of the equipment required. Having a record of the microstructure of each part would enable a new “smart” mass-manufacturing paradigm, where processing is tailored to the microstructure of individual parts in live time [35]. For education and academic research, the low economic barrier to entry makes this technique accessible to institutions that are unable to afford the capital investment of an EBSD-equipped electron microscope. The simplicity, low cost, and enhanced sample throughput of DRM compared to existing techniques promises to vastly expand the availability of crystallographic orientation mapping.

Acknowledgements

The authors would like to acknowledge Le Tan Phuc and Wang Yulai for designing and manufacturing the motorized stage used for DRM measurements; Jude Emil Fronda for his support with MATLAB; Li Bingrui Joel for providing the silicon sample; David J. Srolovitz and Michael J. Demkowicz for insightful discussion. This research was

funded by the Ministry of Education of Singapore, Official Number: MOE2017-T2-2-119. Access to shared experimental facilities used for the experiments described in this work was provided by the School of Mechanical and Aerospace Engineering at NTU.

References

[1] U.F. Kocks, C.N. Tomé, H.R. Wenk, Texture and anisotropy: preferred orientations in polycrystals and their effect on materials properties, 2000.
[2] E.O. Hall, The Deformation and ageing of mild steel: {iii} discussion of results, Proc. Phys. Soc. Sect. B. 64 (1951) 747–753, doi: 10.1088/0370-1301/64/9/303.
[3] N.J. Petch, The cleavage strength of polycrystals, J. Iron Steel Inst 174 (1953) 25–28.
[4] S. Suresh, R.O. Ritchie, Propagation of short fatigue cracks, Int. Met. Rev. 29 (1984) 445–473, doi: 10.1179/imtr.1984.29.1.445.
[5] J. Suryawanshi, K.G. Prashanth, S. Scudino, J. Eckert, O. Prakash, U. Ramamurty, Simultaneous enhancements of strength and toughness in an Al-12Si alloy synthesized using selective laser melting, Acta Mater 115 (2016) 285–294, doi: 10.1016/j.actamat.2016.06.009.
[6] K. Fujiwara, W. Pan, N. Usami, K. Sawada, M. Tokairin, Y. Nose, A. Nomura, T. Shishido, K. Nakajima, Growth of structure-controlled polycrystalline silicon ingots for solar cells by casting, Acta Mater 54 (2006) 3191–3197, doi: 10.1016/j.actamat.2006.03.014.
[7] S. NISHIKAWA, S. KIKUCHI, Diffraction of cathode rays by calcite, Nature 122 (1928) 726, doi: 10.1038/122726a0.
[8] M. Von Heimendahl, W. Bell, G. Thomas, Applications of Kikuchi line analyses in electron microscopy, J. Appl. Phys. 35 (1964) 3614–3616, doi: 10.1063/1.1713282.
[9] A.J. Schwartz, M. Kumar, B.L. Adams, D.P. Field, Electron backscatter diffraction in materials science, Electron Backscatter Diffr. Mater. Sci. (2009) 1–403, doi: 10.1007/978-0-387-88136-2.
[10] F.J. Humphreys, Quantitative metallography by electron backscattered diffraction, J. Microsc. 195 (1999) 170–185, doi: 10.1046/j.1365-2818.1999.00578.x.
[11] G. Wulff, Xxv. zur frage der geschwindigkeit des wachsthums und der auflösung der krystallflächen, Zeitschrift Für Krist. Mater. 34 (1901) 449–530.
[12] G.F. Vander Voort, Metallography, principles and practice, ASM International, 1999.
[13] J. Achard, F. Silva, O. Brinza, X. Bonnin, V. Mille, R. Issaoui, M. Kasu, A. Gicquel, Identification of etch-pit crystallographic faces induced on diamond surface by H 2/O 2 etching plasma treatment, Phys. Status Solidi Appl. Mater. Sci. 206 (2009) 1949–1954, doi: 10.1002/pssa.200982210.
[14] K.A. Bezjian, H.I. Smith, J.M. Carter, M.W. Geis, An Etch Pit Technique for Analyzing Crystallographic Orientation in Si Films, J. Electrochem. Soc. 129 (1982) 1848–1850, doi: 10.1149/1.2124307.
[15] M. Ashikhmin, S. Premože, P. Shirley, A microfacet-based BRDF generator, Proc. ACM SIGGRAPH Conf. Comput. Graph. (2000) 65–74, doi: 10.1145/344779.344814.
[16] M. Seita, M.M. Nimerfroh, M.J. Demkowicz, Acquisition of partial grain orientation information using optical microscopy, Acta Mater 123 (2017) 70–81, doi: 10.1016/j.actamat.2016.10.021.
[17] S. Zhou, M. Seita, Large-area surface topography analysis of additively manufactured metallic materials using directional reflectance microscopy, Mater. Sci. Eng. A 760 (2019) 489–497, doi: 10.1016/j.msea.2019.05.108.
[18] T.B. Britton, J. Jiang, Y. Guo, A. Vilalta-Clemente, D. Wallis, L.N. Hansen, A. Winkelmann, A.J. Wilkinson, Tutorial: Crystal orientations and EBSD - Or which way is up? Mater. Charact. 117 (2016) 113–126, doi: 10.1016/j.matchar.2016.04.008.
[19] Y.H. Chen, S.U. Park, D. Wei, G. Newstadt, M.A. Jackson, J.P. Simmons, M. De Graef, A.O. Hero, A dictionary approach to electron backscatter diffraction indexing, Microsc. Microanal. 21 (2015) 739–752, doi: 10.1017/S1431927615000756.
[20] S. Singh, Y. Guo, B. Winiarski, T.L. Burnett, P.J. Withers, M. De Graef, High resolution low kV EBSD of heavily deformed and nanocrystalline Aluminium by dictionary-based indexing, Sci. Rep. 8 (2018) 1–8, doi: 10.1038/s41598-018-29315-8.
[21] B.L. DeCost, B. Lei, T. Francis, E.A. Holm, High throughput quantitative metallography for complex microstructures using deep learning: A case study in ultrahigh carbon steel, Microsc. Microanal. 25 (2019) 21–29, doi: 10.1017/S1431927618015635.
[22] A. Ryer, Light measurement handbook, 1997.
[23] J. Louthan, Optical Metallography, in: R.E. Whan (Ed.), ASM Handb, 10, ASM International, 1986, pp. 299–308. Mater. Charact.,.
[24] A.T. Polonsky, M.P. Echlin, W.C. Lenthe, R.R. Dehoff, M.M. Kirka, T.M. Pollock, Defects and 3D structural inhomogeneity in electron beam additively manufactured Inconel 718, Mater. Charact. 143 (2018) 171–181, doi: 10.1016/j.matchar.2018.02.020.
[25] Y. Kok, X.P. Tan, P. Wang, M.L.S. Nai, N.H. Loh, E. Liu, S.B. Tor, Anisotropy and heterogeneity of microstructure and mechanical properties in metal additive manufacturing: A critical review, Mater. Des. 139 (2018) 565–586, doi: 10.1016/j.matdes.2017.11.021.
[26] B.C. Salzbrenner, J.M. Rodelas, J.D. Madison, B.H. Jared, L.P. Swiler, Y.L. Shen, B.L. Boyce, High-throughput stochastic tensile performance of additively manufactured stainless steel, J. Mater. Process. Technol. 241 (2017) 1–12, doi: 10.1016/j.jmatprotec.2016.10.023.
[27] M.P. Echlin, A. Mottura, C.J. Torbet, T.M. Pollock, A new TriBeam system for three-dimensional multimodal materials analysis, Rev. Sci. Instrum. (2012) 83, doi: 10.1063/1.3680111.
[28] E.J. Lieberman, A.D. Rollett, R.A. Lebensohn, E.M. Kober, Calculation of grain boundary normals directly from 3D microstructure images, Model. Simul. Mater. Sci. Eng. 23 (2015) 0–18, doi: 10.1088/0965-0393/23/3/035005.
[29] B. Lan, T. Ben Britton, T.S. Jun, W. Gan, M. Hofmann, F.P.E. Dunne, M.J.S. Lowe, Direct volumetric measurement of crystallographic texture using acoustic waves, Acta Mater 159 (2018) 384–394, doi: 10.1016/j.actamat.2018.08.037.
[30] D.H. Hurley, S.J. Reese, F. Farzbod, Application of laser-based resonant ultrasound spectroscopy to study texture in copper, J. Appl. Phys. (2012) 111, doi: 10.1063/1.3692386.
[31] K.-W. Jin, M. De Graef, Correlation of c-Axis Orientation of a-Titanium Grains with Polarized Light Optical Microscopy Intensity Profiles, Microsc. Microanal. 24 (2018) 548–549, doi: 10.1017/s1431927618003239.
[32] D. Lausch, M. Gläser, C. Hagendorf, Determination of crystal grain orientations by optical microscopy at textured surfaces, J. Appl. Phys. (2013) 114, doi: 10.1063/1.4832782.
[33] A. Speidel, R. Su, J. Mitchell-Smith, P. Dryburgh, I. Bisterov, D. Pieris, W. Li, R. Patel, M. Clark, A.T. Clare, Crystallographic texture can be rapidly determined by electrochemical surface analytics, Acta Mater 159 (2018) 89–101, doi: 10.1016/j.actamat.2018.07.059.
[34] O. Ilchenko, Y. Pilgun, A. Kutsyk, F. Bachmann, R. Slipets, M. Todeschini, P.O. Okeyo, H.F. Poulsen, A. Boisen, Fast and quantitative 2D and 3D orientation mapping using Raman microscopy, Nat. Commun.(n.d.)1–10. doi:10.1038/s41467-019-13504-8.
[35] F. Tao, J. Cheng, Q. Qi, M. Zhang, H. Zhang, F. Sui, Digital twin-driven product design, manufacturing and service with big data, Int. J. Adv. Manuf. Technol. 94 (2018) 3563–3576, doi: 10.1007/s00170-017-0233-1.
[36] M. Seita, M. Volpi, S. Patala, I. McCue, C.A. Schuh, M.V. Diamanti, J. Erlebacher, M.J. Demkowicz, A high-throughput technique for determining grain boundary character non-destructively in microstructures with through-thickness grains, Npj Comput. Mater. (2016) 2, doi: 10.1038/npjcompumats.2016.16.